Asociación Argentina
de Mecánica Computacional

Mecánica Computacional Vol XXXI, págs. 823-839 (artículo completo)
Alberto Cardona, Paul H. Kohan, Ricardo D. Quinteros, Mario A. Storti (Eds.)
Salta, Argentina, 13-16 Noviembre 2012

MODELING OF A LIFTING SURFACE WITH AN ACTIVE SMART FLEXIBLE FLAP

Nicolás G. Tripp[a,c], Sergio Preidikman[b,c], Anibal E. Mirasso[a]

[a]*IMERIS,Facultad de Ingeniería, Universidad Nacional de Cuyo, Parque General San Martín, 5501 Mendoza, Argentina, aemirasso@uncu.edu.ar*

[b]*Departamento de Estructuras, Facultad de C. E. F. y N., Universidad Nacional de Córdoba, Casilla de Correo 916, 5000 Córdoba, Argentina, spreidikman@efn.uncor.edu*

[c]*Conicet CCT Mendoza, ntripp@mendoza-conicet.gob.ar*

Keywords: Wind Energy, Smart Blades, Aeroservoelasticity, Piezoelectric transducers.

In the past years, the consumption of energy produced by wind turbines had an exponential growth. This requirement gave momentum to the development of larger turbines with the goal of producing more energy at the same site, reducing the initial investment, and the operation and maintenance costs. In order to achieve this objective, longer, lighter, maintenance-free blades are required so that smaller loads are transferred to the other, more expensive, wind turbine components. The resulting larger flexibility, imposes new challenges to the blade and controller designs; henceforth, new concepts are being developed to add more intelligence into these systems. During the last few years, the electronics industry had invested resources into the research and development of practical applications for piezoelectric ceramic materials. The result of this effort was the development of high precision piezoelectric actuators and sensors, which achieve forces and deformations that are compatible with the ones needed for the control of aerodynamic surfaces. In a former work by the authors, the aeroservoelastic behavior of a two dimensional (2D) wind turbine typical section with an active smart flexible flap was studied. In that work, the potential vibration control properties of an active flexible flap were exposed. In the present work, the study is extended to the three dimensional (3D) space. The flap is modeled as a flexible trailing edge, excited by a piezoelectric actuator, which allows the active morphing of the aerodynamic profile. Structurally, the flap is modeled as a continuum plate, with fixed-free boundary conditions and a piezoelectric actuator at its surface. The flap deflection, relative to the blade surface, is described by the assumed modes method. The flap bending modes are excited actively by means of a commercial piezoelectric actuator. Aerodynamically, the blade-flap system is modeled using an unsteady version of the vortex lattice method. In this model it is assumed that the viscous effects are confined at the boundary layer attached to the surface and the wake shed by the surface. The wake is modeled with vortex rings and it is allowed to move force-free. To capture the physical aspects from the control-fluid-structure interaction, the models are combined using a strong coupling technique. The equations of motion of the system are integrated numerically and interactively in the time domain. In addition, the stability and sensitivity of the system for input perturbations are analyzed. The results show the feasibility of using this type of system in large horizontal axis wind energy turbines.

1 INTRODUCTION

The consumption of renewable energy produced by wind turbines had an exponential growth during last years. The development of large wind turbines producing more energy at the same site reducing the initial investment, the operation and maintenance costs, is an engineering challenge. In order to achieve this objective, longer, lighter, maintenance-free blades are required so that smaller loads are transferred to the other wind turbine components. The resulting larger flexibility imposes new challenges to the blade and controller design. Therefore new concepts are being developed to obtain better systems.

There are several studies regarding this subject, mostly of them applied to aircraft and wind turbines. A good review can be seen in Barlas and Kuik (2010). In this work they highlight that "...trailing edge flap control seems to be one of the most efficient of the proposed aerodynamic control surfaces..".

The modeling of a lifting surface with an active smart flexible flap is not a simple task. Nonlinearities arise due to the offset of shear, tension and mass centers; but also by the Fluid Structure Interaction (FSI). The aerodynamic pressure responds to the shape of the flexible surface; which is in turn a function of the aerodynamic pressure. Moreover the unsteady flow around the blade gives rise to a wake that continuously modifies the pressure field around it. Finally, adding a flexible trailing edge, capable of modifying its own geometry by means of a piezoelectric effect, reveals the full complexity of the problem.

An efficient way for considering the aerodynamic effects is the unsteady vortex lattice method (UVLM) used by Preidikman (1999) and Gebhardt (2008) among others. The former to study the fluid structure interaction in smart wings; and the latter a large horizontal axis wind turbines (LHAWT) behavior.

Embedding an active layer of piezoelectric ceramic material over a layer of a passive material, allows a smooth bending control surface that prevents flow detachment. Pinkerton et al (1997) experimented on a thin layer composite-unimorph ferroelectric driver and sensor (THUNDER) piezoelectric actuator designed by NASA. Buhl et al (2007) studied the use of a THUNDER actuator as a trailing edge flap control for a wind turbine blade. A study on the aeroservoelastic behaviour of a wind turbine blade typical section, equipped with a smart flap, driven by a THUNDER actuator, has been recently presented by the authors (Tripp et al. (2011)). The potential used of piezoelectric control devices in the flap of a typical section is discussed. The results show that adding a simple plunge velocity feedback control law in the piezoelectric layers can increase bending damping up to 73% for the two dimensional case.

In this work, the aeroservoelastic behavior of a three dimensional wind turbine blade approximation, equipped with an active smart flap, is numerically simulated in the time domain. The aerodynamic effects are modelled with the UVLM, and the structural behaviour with the assumed modes method. The latter is widely used in the helicopter industry and in some of the most popular aeroelastic codes for wind turbines, such as FAST (2005).

To capture the physical aspects from the control-fluid-structure interaction, the models are combined using a strong coupling technique. The equations of motion of the aeroservoelastic system are integrated numerically and interactively in the time domain.

First, the model is validated against an experiment found in textbooks. Next, the case of a 100m wind turbine blade-flap undergoing plunging motion is simulated and finally, the results are presented and discussed.

2 AEROSERVOELASTIC MODEL

In this section the aeroservoelastic model is described. First the structural model is presented which comprises an Euler-Bernoulli beam model for the elastic axis and a piezoelectric material model for the flap. Next the UVLM model is presented along with the force generalization. Then the system of equations is shown. Finally the method of solution is presented.

2.1 Coordinate systems and nomenclature:

$\hat{n}_1, \hat{n}_2, \hat{n}_3$: inertial (Newtonian) system.
$\hat{b}_1, \hat{b}_2, \hat{b}_3$: body system that rotates with the local torsion angle.
h is the flexural displacement.
y is the position along the span.
θ is the torsional displacement.
v is the flap deflection relative to the B system.
m is the airfoil section lumped mass.
d_1 is the offset of the center of mass from the shear center.

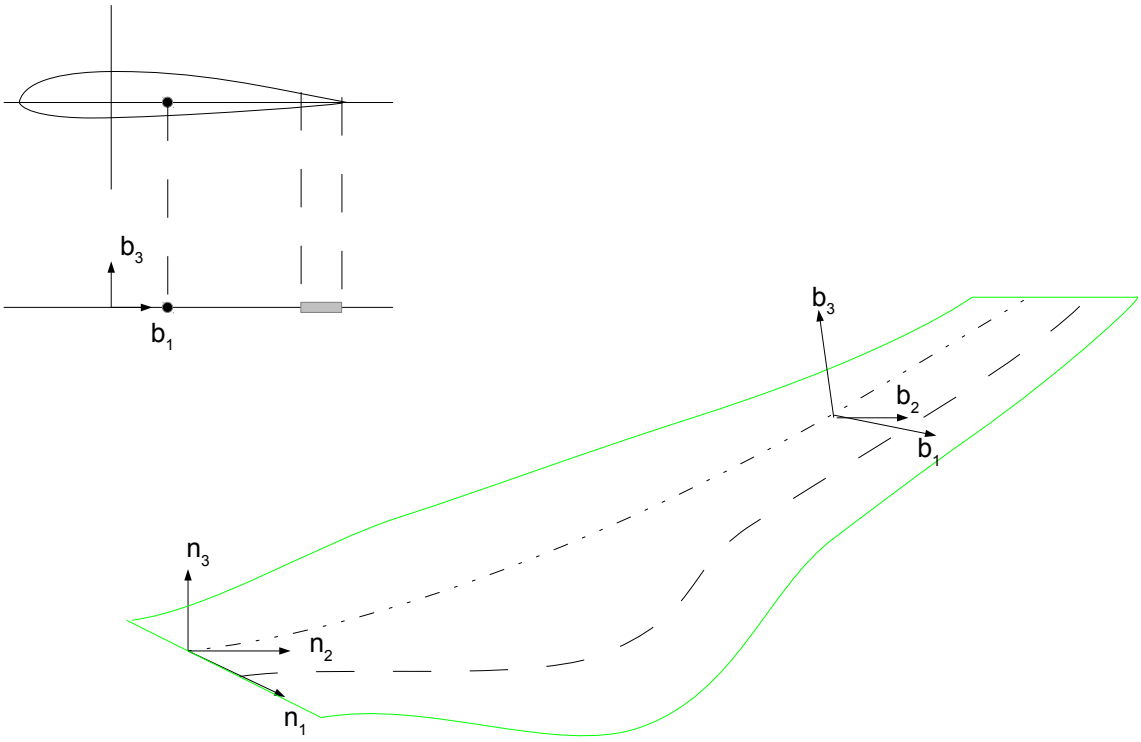

Figure 1: Model Layout

2.2 Structural model

2.2.1 Blade model:

The blade is structurally modeled as a slender beam with its mass lumped at the mass axis. The mass axis is allowed to be displaced from the elastic axis. Only out of plane and torsional

displacement are modeled.
The position vector of a point at the mass axis ($\vec{R}$) is given by:

$$\vec{R} = d_1 \hat{b_1} + y\,\hat{n}_2 + h\,\hat{n}_3 = d_1 \cos\theta\,\hat{n}_1 + y\,\hat{n}_2 + (h - d_1 \sin\theta)\,\hat{n}_3 \tag{1}$$

And its velocity:

$$\dot{\vec{R}} = -d_1\,\dot{\theta}\sin\theta\,\hat{n}_1 + (\dot{h} - d_1\,\dot{\theta}\cos\theta)\,\hat{n}_3 \tag{2}$$

The flexural (h) and the torsional (θ) displacements are described with the assumed modes method, where q_h and q_θ are the modal factors and ψ_h and ψ_θ are the shape functions, for the flexural and torsional modes respectively:

$$\begin{aligned} h(y,t) &= q_h(t)\varphi_h(y) \\ \theta(y,t) &= q_\theta(t)\varphi_\theta(y) \end{aligned} \tag{3}$$

The blade kinetic energy is:

$$T_{blade} = \frac{1}{2}\int_{blade} \dot{\vec{R}}\cdot\dot{\vec{R}}\;\; dm \tag{4}$$

where dm is a differential mass of the blade.

Hence, introducing (2) and (3) into (4):

$$T_{blade} = \frac{1}{2}\dot{q}_\theta^{\,2}\int_{blade}\varphi_\theta^{\,2} d_1^2\, dm + \frac{1}{2}\dot{q}_h^{\,2}\int_{blade}\varphi_h^{\,2}\, dm - \dot{q}_h\dot{q}_\theta\int_{blade}\varphi_h\varphi_\theta d_1\cos(q_\theta\varphi_\theta)\, dm \tag{5}$$

The potential energy for elastic beams with bending and torsion is:

$$U_{blade} = \frac{1}{2}\int_{blade}\sigma\varepsilon\, dvol + \frac{1}{2}\int_{blade}\tau\gamma\, dvol \tag{6}$$

where:
σ and ε are the axial stress and strain of the beam.
τ and γ are the torsional stress and angular distortion of the beam.

Considering Euler-Bernoulli hypothesis and torsion of solid bars:

$$U_{blade} = \frac{1}{2}q_h^{\,2}\int EJ\left(\frac{\partial^2}{\partial y^2}\varphi_h\right)^2 dy + \frac{1}{2}q_\theta^{\,2}\int GJ\left(\frac{\partial}{\partial y}\varphi_\theta\right)^2 dy \tag{7}$$

where EJ and GJ are the section flexural and torsional stiffnesses.

2.2.2 Flap model:

The flap is modeled as a mass-less surface, with fixed-free boundary conditions. The flap deflection, relative to the body of the blade, is described using the assumed modes method, where the displacement field can be described by the superposition of an infinite number of shape functions weighted by coefficients that are functions of time. In this work only one mode is used, as follows:

$$v(x,t) = \varphi_{v(x)}\,q_v(t) = x^2\,q_v(t) \tag{8}$$

where q_v and ψ_v are the modal factor and shape function respectively, and x is the coordinate along the b_1 axis..

2.2.3 Piezoelectric material model:

In this work, following Preidikman et al (2006), a simple linear model is used. It is assumed that the piezoelectric layer is polarized in its thickness direction. The free deformation (Λ) is given by:

$$\Lambda = \frac{d}{t_c} V \tag{9}$$

where:
d is a material constant that defines the piezoelectric strength;
t_c is the thickness of the layer; and
V is the control voltage.

The actuator is a composite material where the bottom layer is made from steel and the upper layer is made from a piezoelectric PZT ceramic. The beam has fixed-free boundary conditions and its bending deflection is approximated by equation (8).

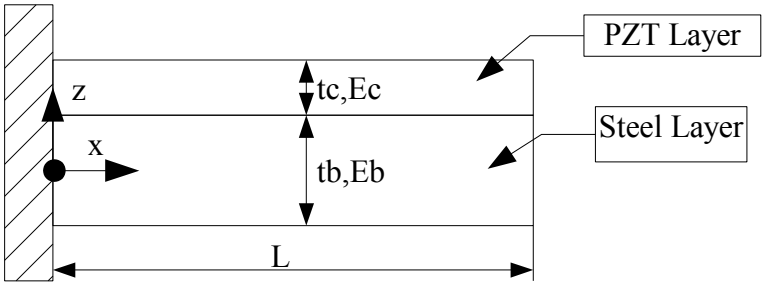

Figure 2: Flap Layout

The strain energy of the flap is given by,

$$U_{flap} = \frac{1}{2}\int_{flap} \sigma\,\varepsilon\, dvol = \frac{1}{2}\int_0^{L_{blade}} \int_0^{c_{(y)}} \int_{z_{min}}^{z_{max}} E_{(z)}\,\varepsilon^2_{(x,z,t)}\; dz\, dx\, dy \tag{10}$$

Euler-Bernoulli slender beam hypotheses are considered and only the strain from pure bending is included.

$$\varepsilon_{(x,z,t)} = -(z - z_e)\frac{\partial^2}{\partial x^2} v_{(x,t)} + \Lambda = -(z - z_e)\, v''_{(x,t)} + \Lambda$$

$$z_e = \frac{E_c t_c (t_b + \frac{t_c}{2}) + E_b t_b (\frac{t_b}{2})}{E_c t_c + E_b t_b} \tag{11}$$

where z is a coordinate along the b_3 axis and z_e is the section centroid.

Combining (8) and (11) results in:

$$\varepsilon^2_{(x,z,t)} = (z - z_e)^2 (\varphi''_{v(x)} q_{v(t)})^2 - 2(z - z_e)\varphi''_{v(x)} q_{v(t)} \Lambda + \Lambda^2 \tag{12}$$

And finally:

$$U_{flap}=\frac{q_v^2}{2}EJ\int_0^{L_{blade}}\int_0^{c_{(y)}}\varphi''^{\,2}_{v(x)}\,dx\,dy-q_v\Lambda ES\int_0^{L_{blade}}\int_0^{c_{(y)}}\varphi''_{v(x)}\,dx\,dy+\frac{\Lambda}{2}E_e\int_0^{L_{blade}}\int_0^{c_{(y)}}dx\,dy \tag{13}$$

$$EJ=\int_{z_{min}}^{z_{max}}E_{(z)}(z-z_e)^2\,dz$$

$$ES=\int_{t_b}^{t_c+t_b}E_{(z)}(z-z_e)\,dz$$

$$E_e=\int_{t_b}^{t_b+t_c}E_{(z)}\,dz$$

2.3 Unsteady Aerodynamics:

A thorough explanation of this model can be found in Katz and Plotkin (1991).

The surface is modeled assuming the hypotheses of thin airfoil theory; that is, as a vortex sheet attached to the airfoil mean camber line. Since only the out of plane bending moment and torsional moment are of interest, the thickness effect, which induce in-plane bending moment is not taken into account. It is assumed that the flow surrounding the surface and its wake is inviscid, irrotational and incompressible, hence there is a velocity potential Φ that fulfills the Laplace equation, which describes its spatial distribution:

$$\nabla^2\Phi=0 \tag{14}$$

In order to have a unique solution, three additional conditions must also be satisfied:

1. The flow is tangent to the airfoil boundaries (zero normal flow):

$$(\nabla\Phi+\vec{v})\cdot\vec{n}=0$$
$$\vec{v}=-[\vec{v}_\infty+\vec{v}_{body}] \tag{15}$$

   where v_∞ is the inflow velocity vector and v_{body} is the surface velocity.
   $\vec{n}$ is the surface normal vector.

2. The flow disturbances vanish far from the body:

$$\lim_{d\to\infty}\nabla\Phi=0 \tag{16}$$

3. The total circulation is constant for all t:

$$\frac{d}{dt}\Gamma=0 \tag{17}$$

The second and third conditions are fulfilled by selecting the vortex ring solution, where the surface and wake sheet are discretized with panels as the one shown in figure 3.

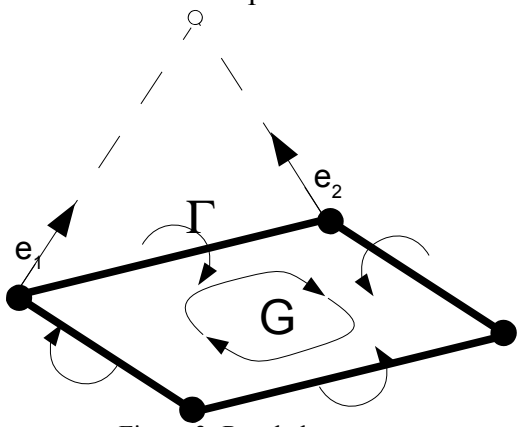

Figure 3: Panel element

The induced velocity is evaluated at the control point located at the ring center. The velocity induced by a single vortex segment at the control point can be written in the following matrix form:

$$\nabla\Phi=\begin{pmatrix}u\\v\\w\end{pmatrix}=\frac{\Gamma}{4\pi}\frac{L\times r_1}{\|L\times r_1\|_2^2}\left(L\cdot\left(e_1-e_2\right)\right)=\vec{a}_{ij}\Gamma \tag{18}$$

where Γ is the segment vortex strength,e_1 and e_2 are diretor cosines, r_1 is the distance in the e_1 direction and L is the segment length. $\vec{a}_{ij}$ Is the aerodynamic influence coefficient which represents the induced velocity for a vortex of a unitary strength. The ring vortex strength is defined as G.

Now the velocity potential can be divided into an airfoil potential and a wake potential.

$$\Phi=\Phi_{airfoil}+\Phi_{wake} \tag{19}$$

Replacing (19) into (15) results:

$$\begin{aligned}&\left(\nabla\Phi_{airfoil}+\nabla\Phi_{wake}-\vec{v}_\infty-\vec{v_{body}}\right)\cdot\vec{n}=0\\&\rightarrow\nabla\Phi_{airfoil}\cdot\vec{n}=-\left(\nabla\Phi_{wake}+\vec{v}_\infty+\vec{v_{body}}\right)\cdot\vec{n}\end{aligned} \tag{20}$$

And taking into account that the total potential at any point is the sum of all the vortex contributions:

$$\nabla\Phi_{airfoil(i)}=\sum_j\vec{a}_{ij}\Gamma_{airfoil(i)} \tag{21}$$

Results in the following algebraic system:

$$A\,\Gamma_{airfoil}=-\left(\nabla\Phi_{wake}+\vec{v}_\infty+\vec{v_{body}}\right)\cdot\vec{n} \tag{22}$$

where A is the matrix of aerodynamic influence coefficients:

$$A_{(ij)}=\left(\sum_j\vec{a}_{ij}\right)\cdot\vec{n}_i \tag{23}$$

At each time step, the linear system of algebraic equations is solved in order to evaluate the circulation around the surface. Having defined the system completely, the induced velocities at the surface and its wake are then calculated. Having this information, the airfoil tangential velocities and pressures are determined using the unsteady version of the Bernoulli equation.

$$\Delta\,p_j=\rho\left(U_\infty\frac{\Gamma_j}{\Delta\,l_j}+\frac{\partial}{\partial\,t}\sum_1^j\Gamma_k\right) \tag{24}$$

where ρ is the air density.

Once the panel pressures are calculated the wake is reconfigured using the total velocity field; then, time is incremented, and all the previous steps are repeated.

2.3.1 Generalized forces

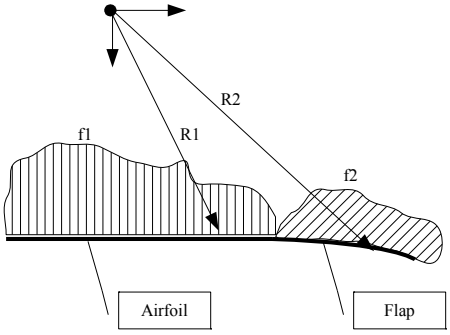

Figure 4: Pressure loads

The virtual work done by the pressure field acting on the blade surface is given by:

$$\delta \bar{W} = \int_{blade} d\vec{f}(x,y,t)\cdot\delta R_1(x,y,t) + \int_{flap} d\vec{f}(x,y,t)\cdot\delta R_2(x,y,t) \tag{25}$$

where:

$$\begin{aligned}
&\vec{df}(x,y,t) = dp(x,y,t)\hat{b}_3 = dp(x,y,t)(\sin\theta\hat{n}_1 + \cos\theta\hat{n}_3)\\
&R_1 = x\cos\theta\hat{n}_1 + y\hat{n}_2 + (h - x\sin\theta)\hat{n}_3\\
&\rightarrow \delta R_1 = -x\sin\theta\delta\theta\hat{n}_1 + (\delta h - x\cos\theta\delta\theta)\hat{n}_3\\
&R_2 = (x\cos\theta + v\sin\theta)\hat{n}_1 + y\hat{n}_2 + (h - x\sin\theta + v\cos\theta)\hat{n}_3\\
&\rightarrow \delta R_2 = ((-x\sin\theta + v\cos\theta)\delta\theta + \delta v\sin\theta)\hat{n}_1 + (\delta h - x\cos\theta\delta\theta + \delta v\cos\theta - v\sin\theta\delta\theta)\hat{n}_3
\end{aligned} \tag{26}$$

Replacing (26) into (25) yields:

$$\begin{aligned}
&\delta\bar{W} = \delta\bar{W}_1 + \delta\bar{W}_2 = Q_h\cdot\delta h + Q_\theta\cdot\delta\theta + Q_v\cdot\delta q_v\\
&Q_h = \int_{blade+flap} \cos\theta\,\varphi_h\, p\, dA\\
&Q_\theta = -\int_{blade+flap} x\,\varphi_\theta\, p\, dA\\
&Q_v = \int_{flap} \varphi_v\, p\, dA
\end{aligned} \tag{27}$$

2.4 Combining the models - equations of motion

The equations of motion are derived using Lagrange equations

$$\frac{d}{dt}\frac{\partial}{\partial \dot{q}_i}(T_{blade})-\frac{\partial}{\partial q_i}(T_{blade})+\frac{\partial}{\partial q_i}(U_{blade}+U_{flap})=Q_i \tag{28}$$

The expressions for the kinetic (equation 5) and potential (equations 7 and 13) energies, along with the expression for the generalized forces (equation 27) are now replaced into equation (28), which can be written in the following matrix form:

$$\begin{bmatrix} m_{hh} & m_{h\theta} & 0 \\ m_{\theta h} & m_{\theta\theta} & 0 \\ 0 & 0 & 0 \end{bmatrix}\cdot\begin{pmatrix} \ddot{h} \\ \ddot{\theta} \\ \ddot{q}_v \end{pmatrix}+\begin{bmatrix} k_{hh} & 0 & 0 \\ 0 & k_{\theta\theta} & 0 \\ 0 & 0 & k_{vv} \end{bmatrix}\cdot\begin{pmatrix} h \\ \theta \\ q_v \end{pmatrix}=\begin{pmatrix} Q_h \\ Q_\theta \\ Q_v+Q_{piezo} \end{pmatrix}-\begin{pmatrix} b_h \\ 0 \\ 0 \end{pmatrix}$$

where

$$\begin{aligned}
&m_{hh}=\int_{blade}\varphi_h^2\,dm \\
&m_{h\theta}=-\int_{blade}\varphi_h\varphi_\theta\,x\cos\theta\,dm \\
&m_{\theta\theta}=\int_{blade}\varphi_\theta^2\,x^2\,dm \\
&k_{hh}=\int_{blade}EJ\,(\varphi_h'')^2\,dy \\
&k_{\theta\theta}=\int_{blade}GJ\,(\varphi_\theta')^2\,dy \\
&k_{vv}=EJ_{flap}\int_0^{L_{blade}}\int_0^{c_{(y)}}(\varphi_{v(x)}'')^2\,dx\,dy \\
&b_h=\dot{q}_\theta^2\int_{blade}\varphi_h\varphi_\theta^2\,x\sin\theta\,dm \\
&Q_{piezo}=\Lambda\,ES_{flap}\int_0^{L_{blade}}\int_0^{c_{(y)}}\varphi_{v(x)}''\,dx\,dy \\
&EJ_{flap}=\int_{z_{min}}^{z_{max}}E_{(z)}(z-z_e)^2\,dz \\
&ES_{flap}=\int_{t_b}^{t_c+t_b}E_{(z)}(z-z_e)\,dz
\end{aligned} \tag{29}$$

2.5 Numerical integration

This system is integrated in the time domain using an explicit-implicit one-step algorithm.

$$\begin{aligned}
&M\,\ddot{q}+K\,\dot{q}=Q-B \\
&\ddot{q}^t=M^{-1}(Q-B-K\,\dot{q}) \\
&\dot{q}^{t+1}=\dot{q}^t+\ddot{q}^t\,\Delta T \\
&q^{t+1}=\dot{q}^t+\ddot{q}^{t+1}\,\Delta T
\end{aligned} \tag{30}$$

The complete algorithm flowchart is as follows:

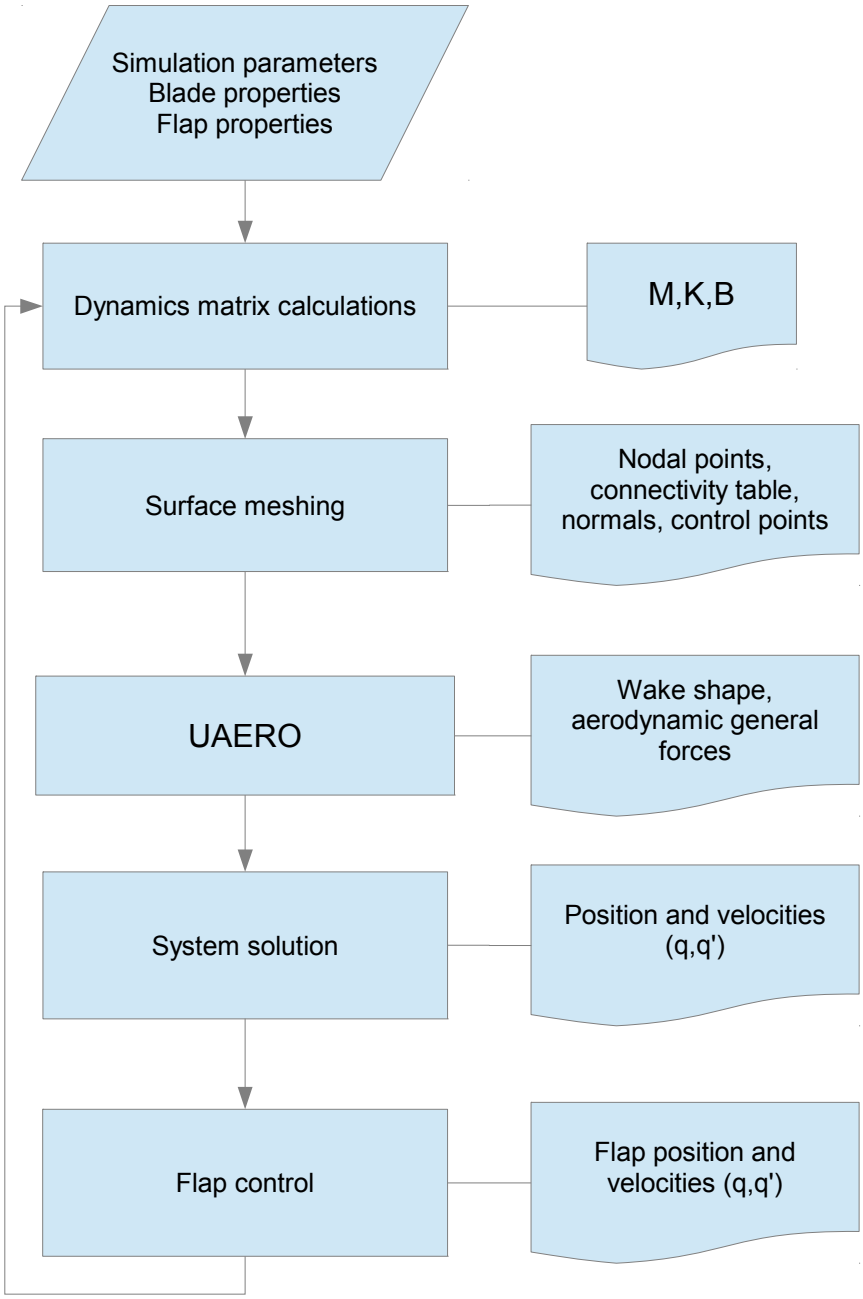

Figure 5: Flowchart

3 RESULTS

3.1 Rigid rectangular wing

A sudden acceleration of an uncambered, rigid, rectangular wing into constant-speed forward flight is considered. The wing has an aspect ratio of 20. The surface is meshed with 4 chordwise and 13 spanwise panels. The wind inflow is set at 10m/s and 5º of angle of attack. This problem is presented in Katz and Plotkin (1991).

In figure 6 the wing geometry and the wake shed are shown. In figure 7 the results from the present model are compared to the reference one showing a close agreement.

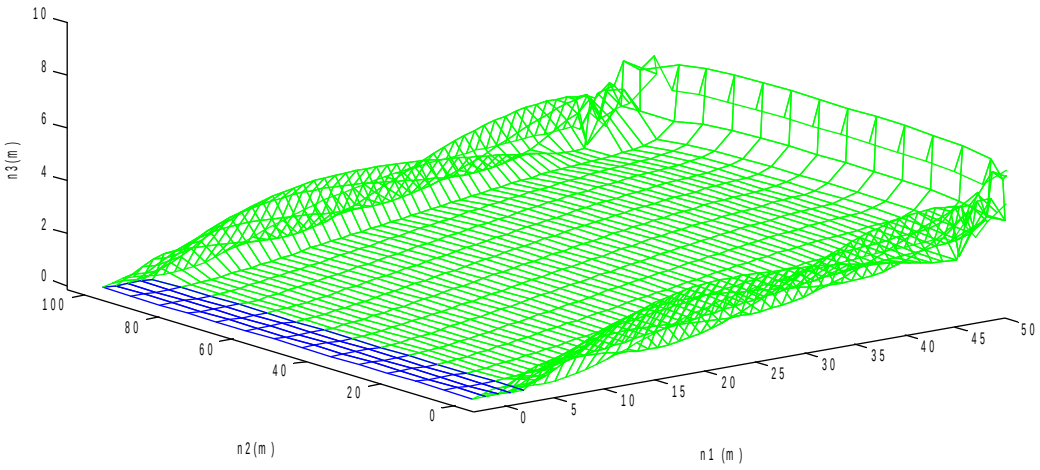

Figure 6: Aerodynamic test model.

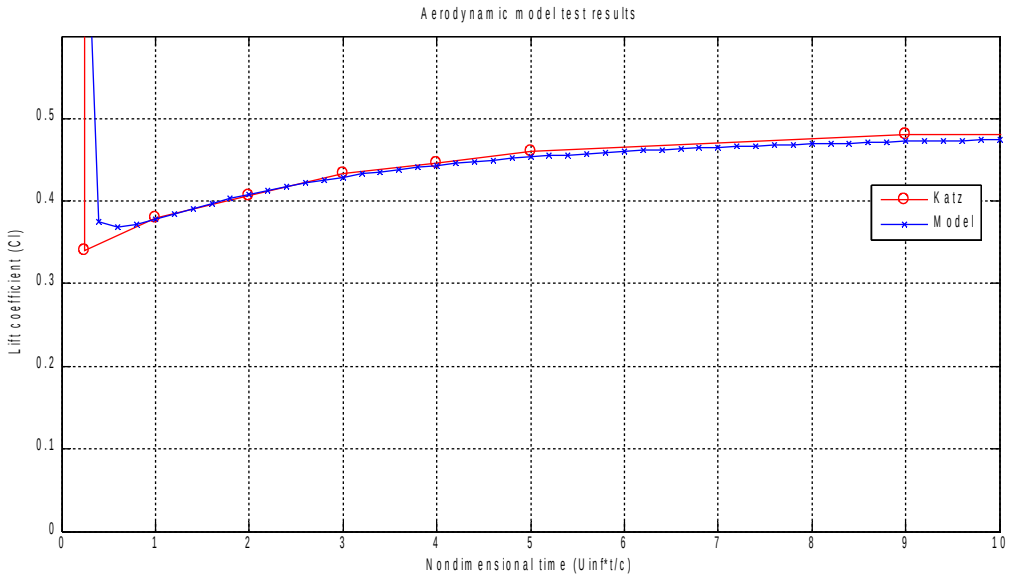

Figure 7: Aerodynamic test results.

3.2 Wind turbine blade

Since the aerodynamic model has been validated in the previous section, a wind turbine blade proposed by the NREL as a reference has been analyzed in this section. The blade chord distribution and structural properties were taken from Griffith and Ashwill (2011), and its length is 100 meters. The blade surface is modeled as an untwisted flat surface with a variable chord. The blade normal modes were extracted from the data using a finite element code written by Bir G. (2012) and distributed by NREL. The modal shapes are shown in figures 8 and 9. For the bending mode there is a good agreement with y^3 but, for the torsional one, the y^2 function was chosen.

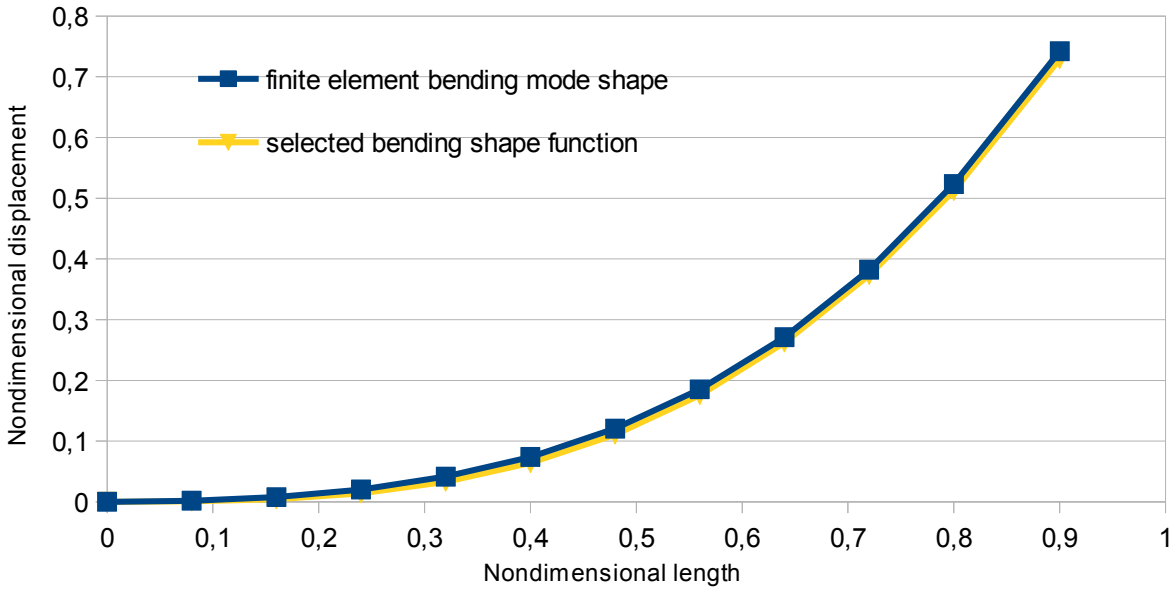

Figure 8: Bending mode.

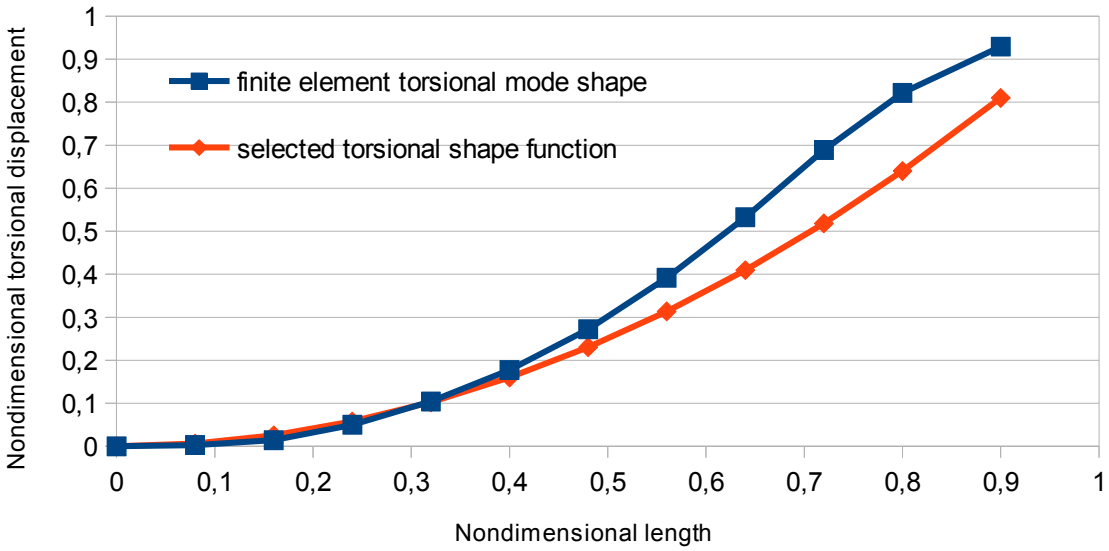

Figure 9: Torsional mode.

For the aerodynamic model the blade is meshed with 10 chordwise and 12 spanwise panels. Since the natural bending frequency is 0.45Hz; while the torsional one is 3.54Hz, the chosen time step for the integration of the coupled systems is 0.03s.

In all the cases an initial displacement of 1m was set in order to force a plunging free motion. The air inflow was set at 10m/s parallel to the X axis. The system setup at the first time step is shown in figure 10.

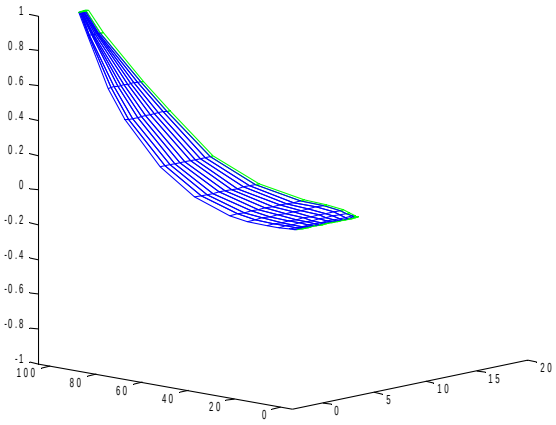

Figure 10: Blade initial configuration, inertial axes are in meters.

3.2.1 Plunging motion for the case without flap

The simulation results are shown in figure 11. The blade geometry and the wake shed by it at the final time step are shown in figure 12.

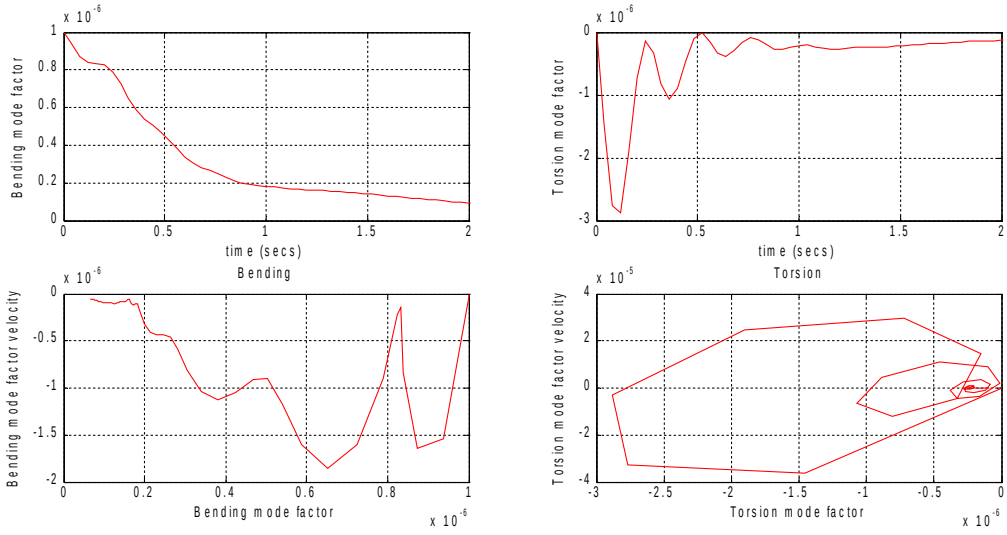

Figure 11: test results.

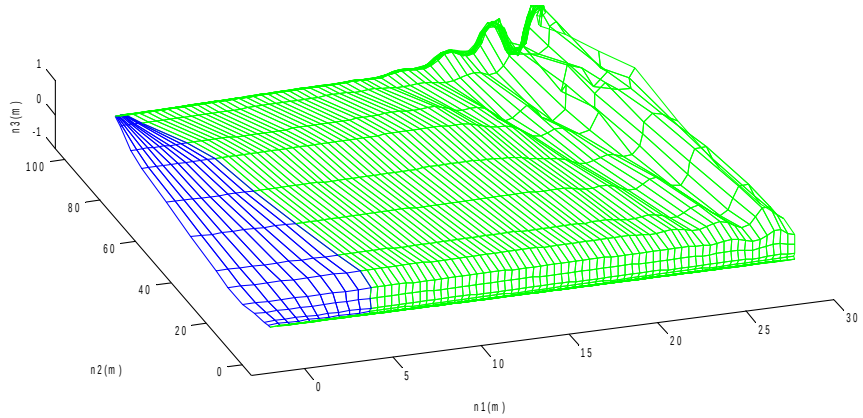

Figure 12: plunging of blade without flap.

3.2.2 Plunging motion for the case with an active deformable flap

In this case, the 100m blade is simulated in the same initial conditions but with the active flap. A simple plunge velocity feedback was defined for controlling the flap.

$$V = -\beta \cdot \dot{h} \tag{31}$$

where:

V is the input voltage for the piezoelectric actuator.

β is the feedback gain.In this test β was taken as 100.

$\dot{h}$ is the plunge velocity

The properties of the piezoelectric and support layers were taken from a data sheet of a commercially available actuator (see THUNDER datasheet). The flap length was defined to be 10% of the local chord for the complete blade span.

The simulation results are shown in figure 13. The blade geometry and the wake shed by it at the final time step are shown in figure 14.

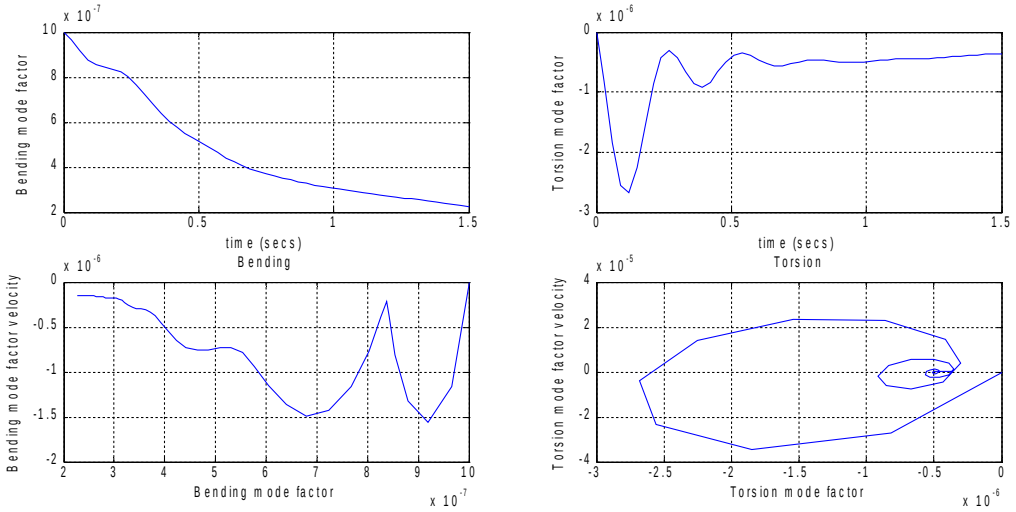

Figure 13: test results.

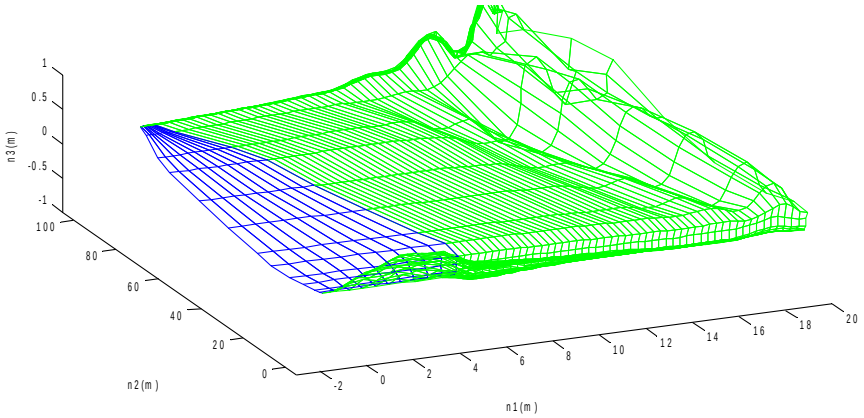

Figure 14: plunging of smart blade.

3.3 Results comparison

The results from the plunge tests are shown as time series in figure 15 and state-space in figure 16. For comparison, the blade response without the flap and without the UVLM is also shown and is designated as "in vacuum", since the aerodynamic effect is not modeled. Due to the system natural frequencies and the simulation length, the system response in vacuum does not complete a full cycle in bending. The results are shown through the generalized coordinates, q_h (bending) and q_θ (torsion).

When comparing the blade response in vacuum to the ones including the UVLM, it can be seen that there is a considerable damping effect from the aerodynamics. Most of the torsional oscillation vanishes in 4-5 cycles depending whether the flap is present or not. In the bending mode there is no oscillation. Therefore damping seems to be larger for the bending mode than for the torsional mode.

From the state-space representation (figure 16) two effects are seen. First, the blade without flap describes a trajectory that is farther from the equilibrium point, than the one with the active flap. This gives a measure of the energy within the system, so the blade with an active flap is dissipating more energy at each cycle. The second effect is that each system converges to a different equilibrium point. Comparing figures 12 and 14, the difference in the equilibrium point is observed in the wake at the blade root. The blade with the deformed flap produces a wake rollup and the other does not.

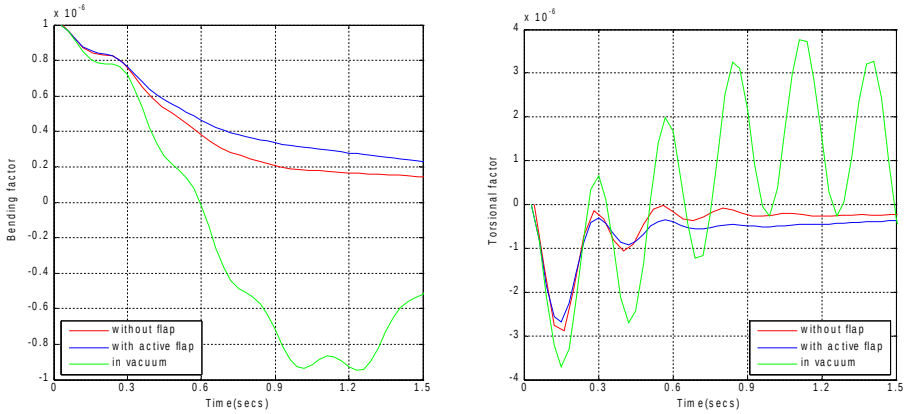

Figure 15: Temporal data.

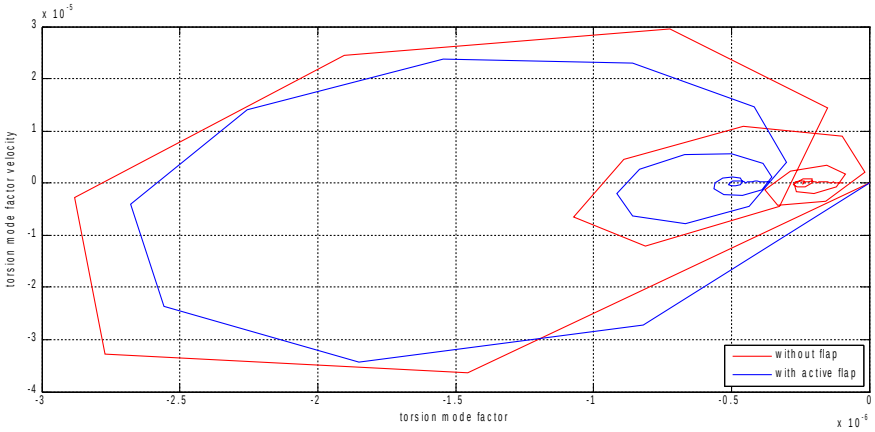

Figure 16: Space-state data.

4 Conclusions

In this work, the aeroservoelastic behavior of a wind turbine blade equipped with an active smart flexible flap is numerically simulated. The unsteady aerodynamic is modeled by means of UVLM. The geometry of the wake is found, iteratively, using a time-stepping technique. The flap is modeled as a multilayered flexible beam with some layers having piezoelectric properties. This allows a control law to be applied evenly over the entire flap. The blade structural response is modeled by the assumed modes method. In this model, the structural damping is not taken into account. The equations of motion of the aeroservoelastic system are integrated numerically and interactively in the time domain using a step-by-step algorithm. The aerodynamic model is validated against a reference case found in textbooks for a rigid flat rectangular wing in steady state condition.

Next, a reference wind turbine blade proposed by NREL with and without an active flap, is simulated in a uniform flow, after an initial displacement is imposed. First, the results show that the three dimensional problem differs from the two dimensional one studied by the authors in a previous work (Tripp et al. (2011)). Bending damping seems to be greater than the one found in the two dimensional version. For the torsional mode, adding a uniform flap with a length of 10% of the local chord, driven by a simple plunge velocity feedback control law, seems to be an effective tool for altering the vibrational response of the blade. There seems to be a difference in the equilibrium points for each case analyzed. This difference could be the result of comparing a blade with a rigid, local chord against one that has a flexible trailing edge and modifies its camber. Observing the state-space visualization, the blade with an active flap seems to be more dampened than the other one.

These results show the feasibility of using this type of system in large horizontal axis wind turbines.

REFERENCES

Barlas T. and Van Kuik G. Review of state of the art in smart rotor control research for wind turbines. *Progress in Aerospace Sciences*,46:1-27,2010.

Bir G. Bmodes. NREL, NWTC Design Codes, http://wind.nrel.gov/designcodes/preprocessors/bmodes, 2012

Buhl T., Bak D., Gaunaa M., Andersen P. Load alleviation through adaptive trailing edge

control surfaces: ADAPWING overview. *EWEA Scientific proceedings*, 20-23,2007.

Face International Corporation, *THUNDER® TH-6R Data Sheet.* http://216.71.30.251/Face%20International/6r-ds.pdf

Gebhardt C., Preidikman S., Massa J., Weber G., Comportamiento aerodinámico y aeroelástico de rotores de generadores eólicos de eje horizontal y de gran potencia. *Mecánica computacional*, 27:519-539, 2008.

Griffith T. and Ashwill T. The Sandia 100-meter All-glass Baseline Wind Turbine Blade: SNL100-00. Sandia National Laboratories. SAND2011-3779,2011

Jonkman J. and Buhl M. FAST User's Guide. National Renewable Energy Laboratory, NREL/EL-500-29798, 2005.

Katz J. and Plotkin A. *LOW SPEED AERODYNAMICS – From wing theory to panel methods*. McGraw-Hill, 1991.

Pinkerton J. and Moses R. A Feasibility Study To Control Airfoil Shape Using THUNDER. NASA, TM-4767,1997

Preidikman S.,Mook D., Time domain simulations of nonlinear, unsteady, aeroelastic behavior. *Mecánica computacional*, 19:361-370,1999.

Preidikman S., Massa J. and Bandi M. Accionamiento mediante actuadores piezoeléctricos de alas flexibles para micro-vehículos aéreos súper maniobrables inspirados en la biología. *Mecánica computacional*, 25:2359-2381,2006.

Tripp N., Preidikman S., Mirasso A. Aeroservoelastic behavior of a wind turbine typical section with an active smart flexible flap. *Mecánica computacional*, 30:2233-2249,2011.